First Study of Sentinel-3 SLSTR Active Fire Detection and FRP Retrieval: Night-time Algorithm Enhancements and Global Intercomparison to MODIS and VIIRS AF Products

Weidong Xu[1,2], Martin J. Wooster[1,2*], Jiangping He[1], Tianran Zhang[1,2]

[1] King's College London, Department of Geography, Aldwych, London WC2B 4BG, UK.

[2] NERC National Centre for Earth Observation (NCEO), King's College London, UK.

Abstract

The Sea and Land Surface Temperature Radiometer (SLSTR) now operates concurrently onboard the European Sentinel-3A and -3B satellites. Its observations are expected ultimately to become the main global source of active fire (AF) detections and fire radiative power (FRP) retrievals for the mid-morning and evening low earth orbit timeslots – data currently supplied by the Moderate Resolution Imaging Spectroradiometer (MODIS) onboard Terra. Here we report for the first-time the significant adjustments made to the pre-launch Sentinel-3 AF detection and fire characterisation algorithm required to optimise its performance with real SLSTR data collected from the Sentinel-3A and -3B satellites. SLSTR possesses both an S7 'standard' and an F1 'fire' channel that operate in the same middle infrared (MIR) waveband, but which use different detectors with differing dynamic ranges and which are located at different focal plane locations. When S7 provides saturated observations, for example over higher FRP active fire pixels, F1 must be used to provide a reliable MIR spectral

* Corresponding author. Tel: +44 (0) 20 7848 2577; Email: martin.wooster@kcl.ac.uk (Martin Wooster)

measurement. However, the two channels differing data characteristics (slightly different size, shape and spatial location of the matching pixels) means that swapping between their measurements is non-trivial. The main algorithm enhancement has therefore been the addition of a dedicated active fire pixel clustering component, required to cluster the detected AF pixels into individual fires as a solution to this issue. Focusing on night-time data due to the added complexity of daytime implementation, we compare AF information derived with this updated SLSTR algorithm to that from near-simultaneous MODIS Terra, and we find that SLSTR has a lower minimum FRP detection limit which enables more lower FRP active fire pixels to be identified than is the case with MODIS. When both sensors detect the same fire cluster at the same time, SLSTR typically measures a slightly higher FRP due to it being able to detect more of the low FRP AF pixels lying at the cluster edge (the OLS linear best fit between matched SLSTR and MODIS per-fire FRP matchups has a slope of 1.08). At the regional scale, SLSTR detects 90% of the AF pixels that the matching MODIS data contains, but also identifies an additional 44% more AF pixels – the vast majority of which have FRP < 5 MW. Regional FRP totals derived from SLSTR appear slightly higher than those from MODIS because of this, and the OLS linear best fit between these regional FRP matchup datasets has a slope of 1.10. Global fire mapping at 1° grid cell resolution for January 2019 shows very similar fire patterns and FRP totals from SLSTR onboard of Sentinel-3B and MODIS Terra, with SLSTR detecting seven times more AF pixels but very similar FRP totals. Case studies in 5° grid cell areas show the same pattern, and longer-term comparisons like these will provide the data required to mesh MODIS and SLSTR data into a single compatible time-series for long-term trend analysis. The night-time SLSTR AF product based on this algorithm has been fully operational from March 2020, available from near real-time feeds and for example through the Sentinel-3 Data Hub (https://scihub.copernicus.eu/s3).

1. Introduction

Landscape burning, including both ‘wildfires’ and ‘controlled burns’, perturb a greater area over a wider variety of biomes than any other natural disturbance agent (Andreae, 1991; Bowman et al.,

2009; Johnston et al., 2011; Reid et al., 2013; Zhang et al., 2018). Fires release smoke containing trace gases and aerosols that significantly impact Earth's atmospheric composition and chemistry, radiation balance, climate and air quality (Natarajan et al., 2012; Van der Werf et al., 2004; Voulgarakis & Field, 2015). The large-scale, sporadic and highly dynamic nature of fire makes satellite Earth Observation (EO) vital for its quantification (Ichoku & Ellison, 2014; Kaiser et al., 2012; Wooster et al., 2015). This extends not only to scientific studies, but also to the need for actionable information to support real-time monitoring and decision making, both in relation to fires on the landscape and to the atmospheric impacts of the emitted smoke (Kaiser et al, 2012, Wooster et al., 2015).

'Active fire' (AF) products are one of the most widely used satellite EO datasets, originally recording the location and timing of fires burning at the time of the satellite observation (Justice et al., 1996; Giglio et al., 2003; 2016) and more recently often adding information on the fires radiative power (FRP) output. This FRP metric has been shown in many studies to be well related to rates of fuel consumption and smoke emission (Wooster et al., 2005; Freeborn et al., 2008; Giglio et al., 2003; 2016; Wooster et al., 2003; Roberts and Wooster 2008, Xu el al., 2010, 2017; Mota and Wooster, 2018), and was first introduced in the widely used Moderate Resolution Imaging Spectroradiometer (MODIS) AF products (Kaufman et al., 1998).

The Sea and Land Surface Temperature Radiometer (SLSTR) is a new spaceborne instrument carried by the European Sentinel-3 satellites sharing some similarities including a similar overpass time to the MODIS instrument operating on the Terra satellite. The AF data produced from SLSTR will be used alongside and ultimately replace those from MODIS Terra, and we report here the novel aspects of an algorithm developed to derive AF detections and FRP retrievals from Sentinel-3, and provide the first comparison between data produced by this algorithm and that from MODIS Terra.

2. Background

SLSTR builds on the heritage of the Along Track Scanning Radiometer (Delderfield *et al.,* 1986), with the first instruments launched as part of the European Union's (EU) Copernicus Programme onboard the Sentinel-3A and Sentinel-3B satellites in 2016 and 2018 respectively. The two satellites provide SLSTR coverage once by day and once by night at most Earth locations, with the exact imaging time on any particular day dependent on the locations' latitude and position within the instrument swath. Imaging is commonly around 10:00 am and 10:00 pm local solar time, similar to that of MODIS Terra which was the first EO instrument that routinely generated global active fire detection and FRP data as part of the MODIS Terra Active Fire and Thermal Anomaly (MOD14) products, now on Collection 6 (Giglio et al., 2003; 2016). The same MODIS AF data have also been generated at different times of day by MODIS Aqua (MYD14), at around 1:30 pm and 1:30 am local solar time. Both MODIS instruments are way beyond their design lifetimes, and at the time of writing that on Terra is more than 20 years old. To preserve fuel, Terra is expected to be placed into a lowered orbit around 2022, altering its local overpass time. The typically strong and biome-dependent fire diurnal cycle causes AF pixel count and FRP to change significantly across a day (Giglio, 2007; Roberts et al., 2009), which can make it difficult to directly combine AF data from markedly different local solar overpass times when trying to assess trends. Active fire data taken around the current MODIS Aqua overpass time are already supplemented, and ultimately will be replaced by, similar-time AF data from the Visible Infrared Imaging Radiometer Suite (VIIRS) sensor operating onboard the Suomi National Polar-orbiting Partnership and subsequent NOAA Polar Orbiting Environmental (POES) satellites (Schroeder et al.,2014; Zhang et al., 2017). Similarly, AF data continuity around the MODIS Terra overpass time is planned to be provided by the four Sentinel-3 spacecraft, the two currently operating and the two further identical versions planned to be launched after 2021, each having a (nominal) 7-year lifetime.

A pre-launch Active Fire and Thermal Anomaly (FTA) algorithm was designed for use with Sentinel-3 SLSTR by Wooster et al. (2012), and its performance evaluated therein using data from MODIS Terra. With both Sentinel-3A and -3B now in orbit, the Wooster et al. (2012) algorithm has now been extensively tested with real SLSTR data, adjusted and optimised as necessary, and a final version 1 post-launch algorithm completed. In the first work to detail active fire detection and FRP retrieval using this new sensor, we here report on the changes made, some of which have involved substantial algorithm enhancements, and on application of the evolved algorithm to real SLSTR data and comparison to the MOD14 MODIS Terra products. The widely used ESA World Fire Atlas (WFA; Arino & Rosaz, 1999) was derived from data taken by the forerunner (Advanced) Along Track Scanning Radiometer instruments ((A)STSR) carried by ERS-2 and ENVISAT. The WFA was restricted to night-time information only because of frequent daytime saturation of the (A)ATSR middle infrared (MIR) band over warm surfaces. Daytime observations by SLSTR face a similar challenge since the sensors nominal-gain MIR channel (S7) also saturates over warm (~ 311 K) surfaces, therefore the AF detection algorithm details require further study. We focus here only on the night-time case, which is that most compatible with the existing ESA World Fire Atlas. The operational Sentinel-3 FRP products based on a night-time processing chain algorithm almost identical to that presented herein have been publicly available in near real-time (NRT) from Eumetsat since March 2020 (https://www.eumetsat.int/website/home/Satellites/CurrentSatellites/Sentinel3/AtmosphericComposition/index.html) and soon after from ESA in non-time critical (NTC) mode using the most up-to date ancillary information (e.g. the atmospheric profiles used for atmospheric correction). Full daytime products will be released in 2021.

3. Sentinel-3 SLSTR Details

The low Earth orbiting Sentinel-3 satellites are aimed at delivering large scale, accurate and timely information on Earth's land, ocean and atmosphere. As detailed by Coppo et al (2010), in addition to

SLSTR each Sentinel-3 carries the Ocean and Land Colour Instrument (OLCI), a microwave radiometer (MWR), Synthetic Aperture Radar (SAR) Altimeter and a Precise Orbit Determination package. Building on (A)ATSR heritage, SLSTR provides dual-view, highly accurate imaging radiometry in multiple channels spanning the visible to longwave infrared spectral range (Llewellyn-Jones et al., 2001). Wooster et al. (2012) provide full details of the overall SLSTR instrument specification with respect to active fire observations, whilst Coppo et al. (2010) provides comprehensive detail on all instrument aspects. The Sentinel-3 AF product is derived from data collected in the SLSTR near-nadir view swath since this offers finer spatial detail and a wider swath width than the oblique view, and SLSTR offers significant advances over ATSR by extending the near-nadir view swath width to ~ 1500 km. It also improves the pixel size of the visible to shortwave infrared (VIS to SWIR) channels to 0.5 km at nadir (retaining ~1 km for standard thermal infrared channels), and adds some further additional spectral channels beyond those of (A)ATSR. The MIR channel is the most important for the active fire application (Wooster et al., 2012), and with MODIS (Giglio et al., 2003) it was found necessary for SLSTR to have two different MIR channels to provide both low-noise, highly radiometrically accurate measurements over ambient temperature targets as well as unsaturated observations over far higher temperature targets. A low-gain 'fire channel' (F1) capable of measuring MIR brightness temperatures in excess of ~450 K was therefore added later in the SLSTR design phase, specifically to provide unsaturated MIR observations over hot targets in the same MIR (3.74 µm) waveband as the 'standard' (S7) MIR channel. Another fire-relevant SLSTR addition beyond (A)ATSR is the 0.5 km spatial resolution 2.2 µm (S6) channel, which is capable of detecting emitted radiance from hot land surface targets at night (Fisher and Wooster, 2019). Finally, SLSTR also possesses an F2 channel operating in the LWIR and capable of measuring higher brightness temperatures than the standard S8 LWIR channel. Both operate in the same 10.8 µm waveband, though at present F2 has not been required to be used for the AF application since the SLSTR active fire detection and FRP retrieval procedure relies only on unsaturated MIR observations (Wooster et al., 2012), and in any case S8 saturation over fires is extremely rare due to there being far less

emissive in the LWIR than in the MIR band (Robinson, 1991). Figure 1 shows that the MIR imagery from the S7 and F1 channels appear similar but not identical, with the data from F1 having a wider dynamic range but also a higher noise level. The SLSTR F1 detectors are actually far smaller than the S7 detectors, and are not co-aligned with them on the instrument focal plane (Coppo et al., 2010; 2015), with some of the implications for active fire observations explained in Wooster et al. (2012). Compared to S7, the F1 data have a different ground pixel footprint shape and size, a smaller pixel area (0.9 km² near nadir compared to the 1 km² of S7), a far more limited growth in pixel area across the near-nadir view scan, as well as a small spatial offset. Together these differences mean that the signal for the same SLSTR pixel measured in the S7 and F1 channels in fact is centred on slightly different ground locations and comes from different footprint areas (Coppo et al., 2010; 2015). Furthermore, due to intricacies in the way the F1 data are calibrated from digital counts to spectral radiance, F1 records anomalously low brightness temperatures (BTs) down-scan of the type of highly radiant pixels characteristic of active fires (Figure 1f). This latter characteristic is reminiscent of a lowered BT anomaly feature seen in the MIR channel on Meteosat Spinning Enhanced Visible and Infrared Imager (SEVIRI) data collected close to active fires, though in that case the cause is digital filtering onboard Meteosat (Wooster et al., 2015). The unsaturated F1 observations over active fires, as well as the smaller pixel area and swath-dependent pixel area growth characteristics of F1, are of significant benefit to the AF application, but the channels' high noise levels, spatial offset and downscan BT anomalies make use of S7 still important, and make use of F1 data in combination with S7 non-trivial. Significant updates to the original pre-launch SLSTR AF detection and FRP retrieval algorithm detailed in Wooster et al. (2012) were required to deal with the joint use of S7 and F1 data.

4. SLSTR Nighttime AF Detection & FRP Algorithm Adjustments

The initial changes to the active fire detection thresholds specified in the pre-launch algorithm of Wooster et al. (2012) were based on detailed examination of early scenes collected by Sentinel-3A

over Canada, America, Europe and Africa and detailed in Appendix A (Table A1; Fig. A1). Other relatively minor adjustments detailed in Appendix A include alteration of certain tests used in the contextual detection stage, removal of the desert boundary rejection test, addition of a dedicated cloud mask and a water and cloud edge mask, and atmospheric correction of the FRP retrievals. The majority of the algorithm remains as described in Wooster et al. (2002) and all the above updates are fully detailed in Appendix A. By far the most significant enhancement to the pre-launch algorithm however is the introduction of clustering of separate AF pixels into individual fires, which is described below and relates to the strategy used to cope with the far more frequent use of the F1 data than initially envisaged for both Sential-3A and -3B due to frequent saturation of S7 caused by its dynamic range plateauing at around 311 K instead of the originally specified 325 K.

Both S7 and F1 have identical MIR channel spectral response functions (Coppo et al., 2010; 2015), but are not spatially co-aligned and have different pixel sizes and shapes as explained in Section 3. S7 offers better AF detection sensitivity due to its lower noise and ability to be used in conjunction with the co-registered S8 channel, so apart from the absolute AF threshold detection test, which identifies the most radiant active fire pixels using a simple F1 channel brightness temperature threshold (see Wooster et al., 2012), all other night-time AF fire pixels are first detected using data from S7. However, when the S7 detector is saturated the AF pixel FRP value cannot be accurately retrieved using these data – so that from the lower-gain F1 channel must be used instead. However, it is not possible to simply swap between use of the S7 and F1 channel data at the level of individual AF pixels, because the two channels are not measuring the signal from exactly the same ground area as explained in Section 3. Instead, for any AF pixel saturated in S7 - all AF pixels spatially contiguous with it (i.e. in an active fire 'cluster') must have their FRP retrieved using the F1 data, and this means finding the cluster of AF pixels in the F1 channel that correspond to the cluster in S7. This is performed by first grouping all the relevant S7 AF pixels into a single AF cluster, searching for the matching cluster in F1, and then deriving the per-pixel FRP from the F1 AF pixels identified to be part of that cluster. Clustering the S7-detected AF pixels in this way minimises computational time in

194 detecting the matching F1 AF pixels, whilst also helping to make their detection more accurate. For
195 example, in Figure 2a there are six AF pixels shown detected in the S7 data. If these six S7-detected
196 AF pixels were each used as seeds for an F1 AF pixel detection scheme based on a simple search
197 window, the search operation would need to be run six times. Each time the search would detect
198 many of the same F1 AF pixels, which would then have to be rationalised into the single set of
199 twelve F1 AF pixels see in Figure 2b. The clustering operation avoids this duplication of
200 computational effort. Furthermore, since the F1 AF pixel detection tests are based on the signal in
201 the F1 channel alone (Step iv below), they can sometimes detect candidate AF pixels in the search
202 window that are spatially unconnected to the AF cluster. The connected component labelling
203 approach contained within the clustering procedure allows such pixels to be removed since they are
204 not part of the identified AF cluster.

205 Because the F1 channel pixel area is smaller and has a lower pixel area growth rate away from nadir,
206 there are some benefits from using the F1 data for all FRP retrievals, even at fires containing only
207 unsaturated S7 observations (Wooster et al., 2012). This is the strategy expected to be deployed
208 operationally, and thus the approach used here. Therefore, in the current work all S7-detected AF
209 pixels have been subject to the clustering approach detailed above, and thus have their AF pixels re-
210 detected and their FRP measured using the F1 data. However, the ambient background radiances
211 required by the FRP retrieval (Wooster et al., 2003; 2005) always come from S7, because this
212 channel has lower noise and is unaffected by the aforementioned down-scan low BT anomalies that
213 affect F1 and which are shown in Figure 1f. Full details of the AF clustering approach are expressed
214 in steps (i) to (vii) below, parts of which are illustrated in Figure 2.

215 (i) AF pixels are detected in the S7 channel using the pre-launch algorithm of Wooster el al. (2012),
216 with minor modifications detailed in Appendix A. These AF pixels are then grouped into individual AF
217 clusters using the connected-component labelling approach of Dillencourt et al. (1992). The method

groups a spatially connected set of AF pixels detected in S7 into a single AF cluster, based on the steps detailed below:

Step 1: The AF pixel detections are used to create a binary image "mask" that has:

V={1} where a pixel is an AF pixel

V={0} where a pixel is not an AF pixel.

Step 2: Starting from the first pixel in the binary image mask. A current label (C) counter is set to 1.

Step 3: If this pixel is an AF fire pixel [i.e. has V={1}] and it is not already labelled with the current label value, then it is given the current label (C), added as the first element in a queue, and the algorithm then proceeds to Step 4. However, if this pixel is not an AF pixel [i.e. has V={0}] or it is already labelled, then Step 2 is repeated for the next AF pixel in the binary mask.

Step 4: An element is extracted from the queue and each of its neighbours in the binary image mask (based on any type of spatial connectivity [up, down, left, right or diagonal] are examined. Each neighbouring pixel that is itself classed as an AF pixel (and which is not already labelled) is given the current label and added to the queue. Step 4 is repeated until there are no more elements in the queue.

Step 5: Step 3 is then checked for the next AF pixel in the binary image mask, and the current label (C) is incremented by 1.

(ii) The mean brightness temperature in the S7 channel ($\overline{BT}_{S7}$) and the mean absolute deviation ($\sigma_{BT_{S7}}$) of the background window BTs surrounding each S7 AF cluster is recorded.

(iii) Each individual AF pixel in the S7 AF cluster is assigned a label identifying it as belonging to the same fire cluster, and the cluster size is calculated as the number of columns and rows (F_x, F_y) that

encompass all AF pixels making up the cluster. For example, for the cluster shown in Figure 2a F_x=4 and F_y=3.

(iv) A search for the matching AF cluster in the F1 channel begins, using a window around the cluster identified in S7. The F1 search window corresponding to an identified S7 AF cluster is centred at the same location as the top left AF pixel in the S7 AF cluster, and has a window kernel size 10 pixels larger than the S7 fire cluster size in each dimension (i.e. a size $(F_x + 10) \times (F_y + 10)$ pixels). We found this window size to be sufficient to account for the spatial offset between the F1 and S7 channel data at any location in the near nadir-view scan. For example, in Figure 2a the kernel size is 14 (=4 + 10) × 13 (=3 + 10)). Each F1 pixel within the window is tested to determine whether or not it is a candidate AF pixel using one of the following tests, depending on its pixel signal and background variability:

$$\{\text{If } \sigma_{BT_{S7}} \geq 1 \text{ then } BT_{F1} > \overline{BT}_{S7} + 3 \times \sigma_{BT_{S7}} \quad (1)$$

$$\text{else if } \sigma_{BT_{S7}} < 1 \text{ then } BT_{F1} > \overline{BT}_{S7} + \sigma_{BT_{S7}} + 2\ \}. \quad (2)$$

Or

$$\{\text{The absolute threshold Test } BT_{F1} > 326 \text{ K is true}\} \quad (3)$$

Where BT_{F1} is the BT from F1 channel; $\overline{BT}_{S7}$ is mean S7 BT of the valid background pixels; and $\sigma_{BT_{S7}}$ is the mean absolute deviation of the S7 brightess temperatures of the valid background pixels.

(v) Also cluster the candidate F1 AF pixels into individual fire clusters, in the same way as was conducted for AF pixels in S7. Identify the individual F1 cluster matching each S7 cluster using the same connected-component labelling method used in (i) (see Figure 2). For example, Figure 2c shows how the clustering approach is used to confirm the candidate AF pixels identified in F1 (blue) as belonging to the same cluster as the AF pixels identified in S7 (red), based on the fact that they

264 are spatially connected. This step removes any candidate F1 AF pixel that is not spatially connected
265 to the others in the cluster under examination. These discounted candidate AF pixels maybe true AF
266 pixels which are not part of the identified cluster, or may even be false alarms coming from the
267 relatively simple F1 AF detection procedure (step iv above).

268 (vi) Calculate the FRP of each AF pixel in the matching F1 cluster, based on the MIR radiance
269 approach (Wooster et al., 2005), the AF pixel spectral radiances measured in F1 and the mean
270 background window radiances measured in S7.

271 (vii) Report the location and FRP of each active fire pixel in the whole fire cluster in the F1 domain.

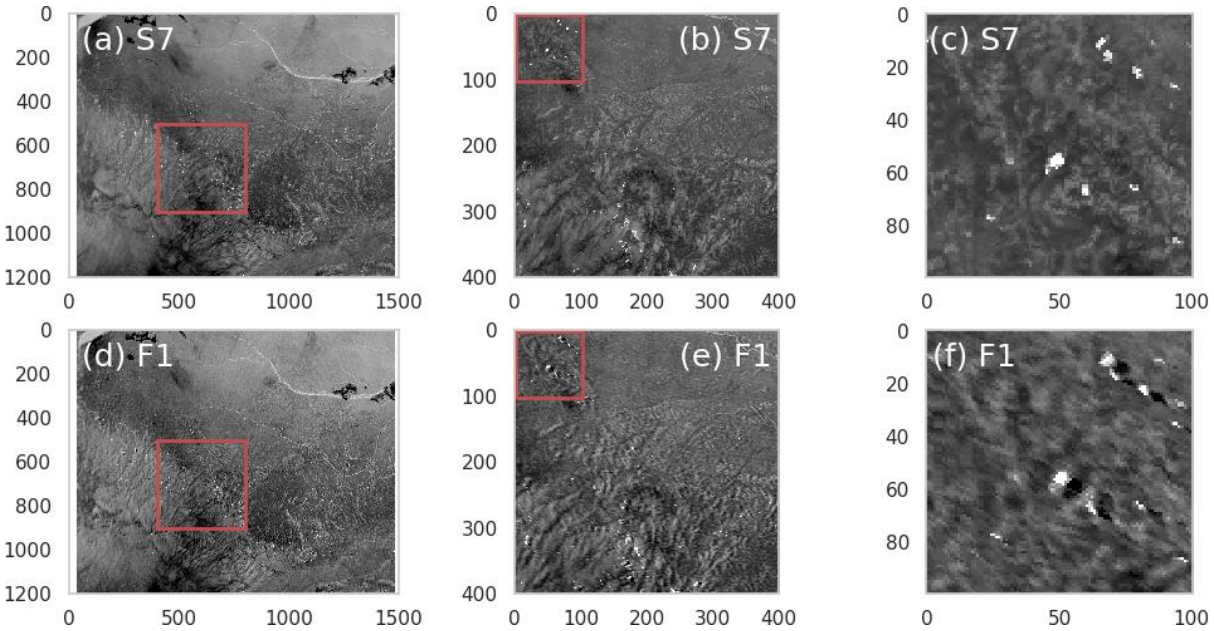

272

273 **Figure 1.** Nighttime SLSTR Level 1b brightness temperature (BT) images of actively burning
274 fires taken by Sentinel-3A over central Africa at 20:27 UTC on 4th January 2018. Each column
275 represents a zoom of the prior columns' information, with data from the 'standard' S7
276 channel (top row) and the 'low gain' F1 fire channel (bottom row) are shown. Both channels
277 measure incoming IR radiation in the same 3.7 µm waveband, but F1 does so across a far
278 wider dynamic range since its gain is optimized for active fire observations (Wooster et al.,
279 2012). Pixels containing fires have elevated BT values and show as bright in this rendition.

280 Whilst the same fires are identified in both channels, the number of active fire pixels and
281 the shape of each fire is a little different between the two channels of data (most easily seen
282 in (c) and (f)), due to differences in the S7 and F1 detector shapes and signal integration
283 times detailed in Coppo et al. (2010) and Wooster et al. (2012). Some active fire pixels are
284 saturated in the S7 data, but the benefit of F1 is that none of them are saturated. However,
285 the F1 data show higher noise over the ambient temperature non-fire background, have a
286 small spatial offset from the matching S7 pixels, and possess anomalously low BT values
287 down-scan of the fires (dark areas to the bottom right of each fire in Figure 1f, which are not
288 present in the S7 data of Figure 1c).

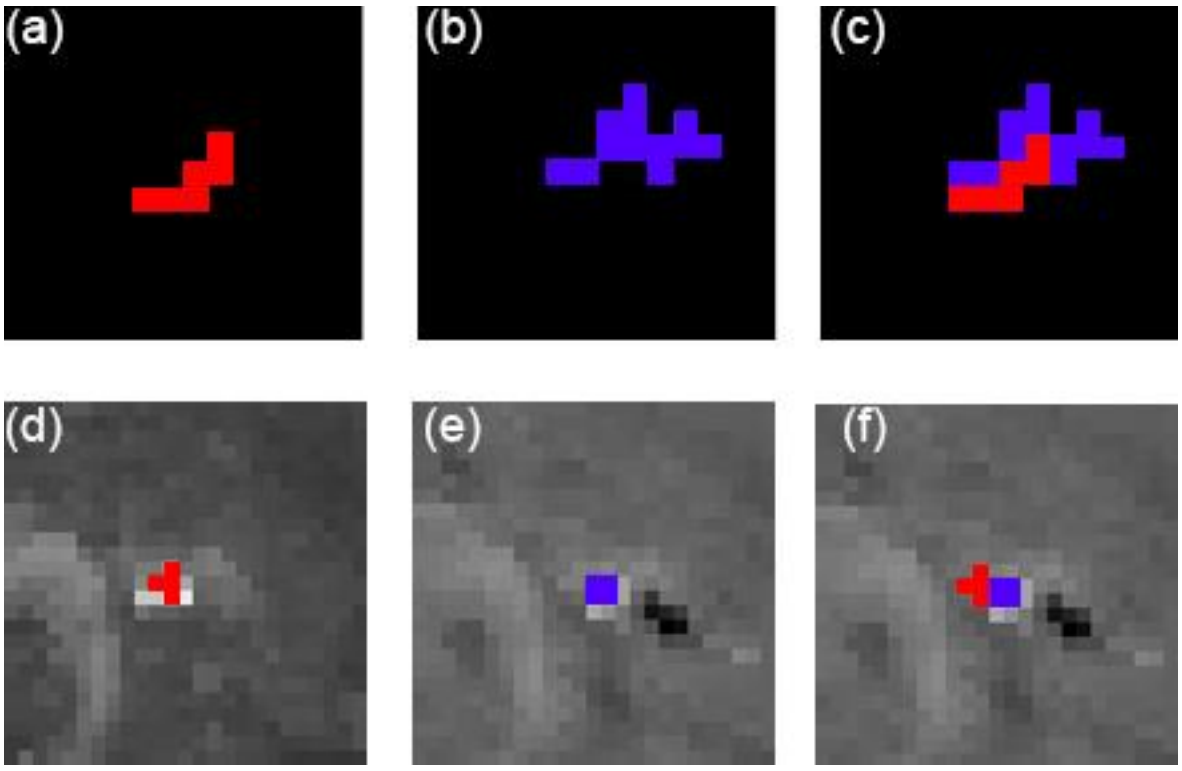

289

290 **Figure 2.** Illustration of the workings of the active fire (AF) pixel clustering approach
291 described in Section 3. Top row shows one example, where the background non-fire pixels
292 are set to zero for clarity and with a zoomed focus only over the active fire location. The red
293 colour indicates the fire pixels detected from S7 and blue denotes the corresponding fire

pixels on F1. (a) Location of AF pixels detected in the S7 channel using the contextual AF detection component of the pre-launch algorithm (detailed in Wooster et al., 2012) and the updated detection thresholds reported in Appendix A; (b) Location of AF pixels (blue) detected in the F1 channel within the kernel centered at upper left fire pixel of the S7-detected AF pixel cluster locations in (a) in red and tests (i) to (v) of Section 4. (c) The detected S7 and F1 AF pixels overlain on the F1 channel data, showing their clearly different locations that result in a different AF cluster shape. Bottom row shows a separate example with the background values maintained and a wider view around a fire (where for example the down scan low-BT anomaly can be seen in the F1 data of (e) and (f), but not the S7 data of (d).

5. Performance Comparison to MODIS, VIIRS and Example Outputs

The updated Sentinel-3 SLSTR AF detection and FRP retrieval nighttime algorithm summarized in Section 4 and appendix A was applied to global Sentinel-3B SLSTR data collected in January 2019, as well as to the Sentinel-3A scenes list in Table A1 (Appendix A). At this time of year, fires are burning strongly across north Africa, northern SE Asia, and other sub-tropical regions (Giglio, 2007). Outputs from the enhanced SLSTR AF detection and FRP retrieval approach detailed herein were compared in detail to the Collection 6 (C6) MODIS Terra AF (MOD14 swath) products, generated using the algorithm of Giglio et al. (2016). The night-time Terra MOD14 AF products are derived from observations made at a similar overpass time to that of Sentinel-3, and thus in some instances it is even possible to directly compare views of the same active fire made at almost identical times from MODIS and SLSTR. The VIIRS sensor carried by the Suomi National Polar-orbiting Partnership (NPP) satellite has a higher spatial resolution than MODIS, and thus typically detects more

AF pixels than MODIS and records a higher FRP across landscapes (Zhang et al., 2017; Li et al., 2020). However, Suomi NPP overpasses many hours later at night than Sentinel-3 and Terra. Since major changes in landscape fire number and intensity can occur in only a few hours (e.g. Giglio et al., 2007; Roberts et al., 2009; Xu et al., 2017) direct comparisons between fires observed by SLSTR and VIIRS are thus not attempted herein. Instead we compare the global gridded SLSTR active fire data to that from the VIIRS 375 m I-Band active fire data product (VNP14IMGTDL) as well as to MODIS Terra to gauge the degree of similarity in the recorded spatial patterns and overall levels of fire activity.

5.1 SLSTR Active Fire Detection Performance Intercomparison Approach

Procedures used to initially compare the Sentinel-3 and MODIS Terra AF products collected at almost the same time of day followed those of Freeborn et al., (2014a), previously used to evaluate the performance of the LSA SAF Meteosat SEVIRI FRP-PIXEL product (Roberts et al., 2015) and other geostationary AF products (e.g. Xu et al., 2010, 2017). Specifically, we used instances of near contemporaneous MODIS and SLSTR data collection, such as that shown in Figure 3. SLSTR AF detection errors of omission and commission with respect to MODIS were calculated, as well as the degree of FRP agreement in two cases (i) when both sensors view the same individual fire cluster at the same time (within ± 6 minutes), and (ii) when both sensors view the same larger land surface region at the same time (within ± 6 minutes). In these comparisons, in addition to requiring near simultaneous-views, the MODIS data were restricted to those with a MODIS scan angle maximum of ±30° to avoid geometric issues associated with the MODIS 'bow-tie' effect (Freeborn et al., 2011; 2014a). This limited the MODIS pixel area to a maximum of 1.7 km², and to match this the SLSTR data were also restricted to those with a S7 channel pixel area maximum of 1.7 km² (the matching F1 pixel area maximum was 1.2 km²). To facilitate the inter-comparison, MODIS AF

pixels were re-projected to the SLSTR Level 1b global Universal Transverse Mercator (UTM) projection data grid, and Sentinel-3 AF errors of omission with respect to MODIS were evaluated by considering whether an SLSTR AF detection was present within a 7 ×7 pixel window centred on each MODIS AF pixel location. This window is larger than the 3×3 originally used by Freeborn et al., (2014a) because of the need to include the additional, spatially variable, spatial offset present between the SLSTR S7 and F1 channel data discussed in Section 2. The reverse approach was used to evaluate the Sentinel-3 SLSTR AF pixel errors of commission.

A matching SLSTR and MODIS example is shown in Figure 3, and in this case SLSTR identifies all AF pixels detected in the C6 MODIS product (a total of 283), plus an additional 67 AF pixels that were undetected by MODIS. These additional AF pixels are either isolated single pixel detections, or pixels lying at the edges of detected AF clusters. As an example, the two AF clusters highlighted by blue rectangles in Figure 3d contain a total of 48 AF pixels, and all but one have an FRP < 5 MW. This is below the standard minimum FRP detection limit for the MODIS AF products, but the SLSTR output is able to include them due to its lower minimum FRP detection threshold that stems from its slightly increased AF detection sensitivity (Wooster et al., 2012) and the smaller nadir pixel area of the F1 band. Figure 3c also shows that at night many fires clearly show up in the 500 m spatial resolution S6 SWIR band, confirming that the AF detections based on the thermal channel data are the result of real fires and not false alarms. Whilst we do not use S6 for AF detection in this work, its use will be implemented in the final operational algorithms.

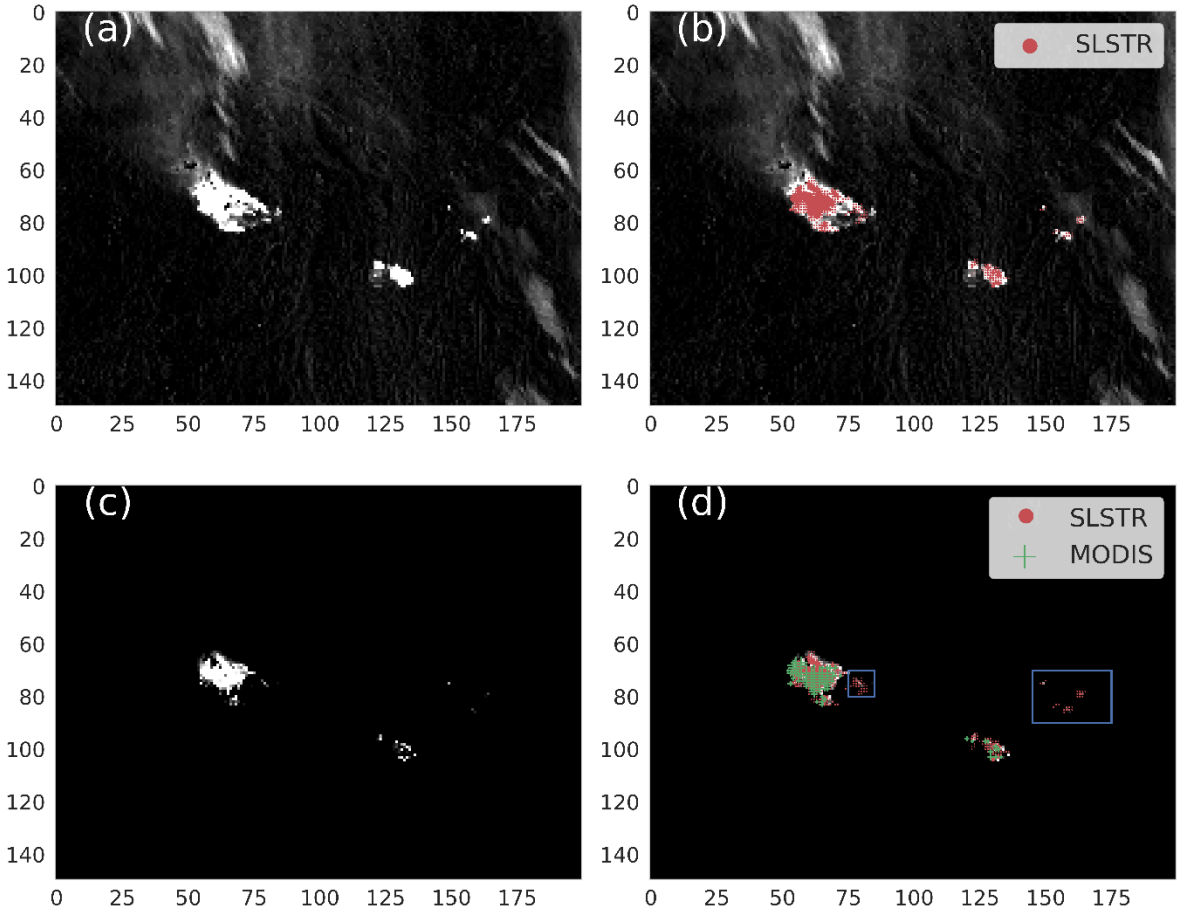

Figure 3. Comparison between near-simultaneous night-time Sentinel-3A SLSTR and MODIS Terra active fire (AF) pixel data of Canada, based on the methodology detailed in Section 4.1. The SLSTR image subset covers 200 km × 150 km and were collected at 04:56 UTC on 6th May 2016, and the matching MODIS data at 05:00 UTC. (a) SLSTR MIR-LWIR Brightness Temperature (BT) difference image calculated using S7 and S8 channel data, and where higher BT differences are depicted as brighter pixels. (b) Same as (a) but with the SLSTR AF detections overlain with a one pixel offset for clarity. (c) SLSTR S6 channel data (SWIR waveband) matching (a), and (d) the same as (c) but with SLSTR AF detections superimposed as red '•' and near-simultaneous MODIS AF detections as green '+' (both with one pixel offsets for clarity). The blue rectangle highlights the AF pixels detected by SLSTR but missed by MODIS.

Beyond the comparisons of near-simultaneous SLSTR and MODIS AF data, a series of additional comparisons were made, based on all Sentinel-3B SLSTR and MODIS Terra AF data collected in January 2019, regardless of pixel area and observation time. The analyses were of FRP frequency-magnitude distribution, total AF pixel count and total FRP on a global 1° grid, and four larger (5°×5°) grid cells at a detailed time series level.

5.2 SLSTR Active Fire Detection Performance Intercomparison Results

Considering the global data of January 2019 overall, a total of 46 MODIS Terra AF products were identified that matched within ±6 minutes of an SLSTR granule containing at least one AF pixel detection. Within the MODIS scan angle limit of 30°, a total of 1,213 MODIS AF pixels were identified, most located in northern hemisphere Africa. Significant numbers of AF pixels were also detected over gas flaring locations in Iraq. 90% of the MODIS AF pixel detections had a matching Sentinel-3 AF pixel detection, representing an apparent 10% MODIS product commission error compared to SLSTR. Conversely, the Sentinel-3 AF products contained 3,786 AF pixels, with only 2,123 (56%) having a matching MODIS AF pixel. Of the additional AF pixels detected by SLSTR, 79% had an FRP $\leq$ 5 MW and so represent AF detections below the minimum MODIS FRP detection limit. These global statistics broadly mirror those differences demonstrated for the single sub-scene matchup of Figure 3.

Pre-launch testing of the original algorithm of Wooster et al. (2012) with MODIS data already indicated that it tended to identify more AF pixels than did the MODIS AF detection algorithm of Giglio et al. (2003), around 30% more in those tests when both algorithms were applied to MODIS level 1b data. Giglio et al. (2016) updated the MODIS AF detection algorithm – in part to enable detection of somewhat lower FRP AF pixels - though some of

398 the tests in the SLSTR algorithm reported herein still use lower thresholds than do the
399 matching MODIS tests, meaning that even when fed with the same data the former maybe
400 able to detect AF pixels having slightly lower FRP values than can MODIS. For example, the
401 SLSTR contextual detection test (Test 6c) of Wooster et al. (2012) uses a 5.6 K MIR-LWIR BT
402 difference threshold, whilst the C6 MODIS algorithm of Giglio et al. (2016) uses a slightly
403 higher 6 K threshold. However, beyond these relatively small threshold differences, two
404 more significant factors contribute to SLSTR's apparent ability to identify more AF pixels that
405 does MODIS. The first is the AF clustering approach detailed in Section 4, and the second is
406 use of the F1 band. For the clustering approach, after a set of AF pixels are identified and
407 then clustered using data from the 'S' channels, the matching F1 AF pixels are identified and
408 clustered using only the F1 data and the two tests detailed in Section 4. This compares to
409 Tests 6a to 6d in Wooster et al. (2012), which are applied to brightness temperature data
410 from S7 and S8 and their difference, and which typically do not identify as many AF pixels as
411 does the simpler and subsequently applied F1 test that also benefits from the smaller pixel
412 area of F1 at any point around the SLSTR scan compared to the S7 and S8 pixels. This F1
413 pixel area is also smaller than MODIS, and grows off-nadir at a smaller rate than that of
414 MODIS (Wooster et al., 2012), further increasing the ability of SLSTR to detect lower FRP
415 active fire pixels than MODIS when both sensors view the same location at the same scan
416 angle.

417 ### 5.3 Evaluation of FRP Retrievals

418 Figure 4 presents results of the FRP retrieval inter-comparison between Sentinel-3 SLSTR
419 and MODIS Terra. Figure 4a presents the per-fire analysis, based on the approach of near-
420 simultaneous views of the same fire cluster previously used by Roberts et al., (2015),

Wooster et al. (2015) and Xu et al. (2010; 2017). The near unity slope (1.08) demonstrates a good degree of agreement between the two measures, with the SLSTR-retrieval being typically higher primarily because its AF product often detects some additional low FRP pixels at the edges of fire clusters than does MODIS. The coefficient of variation (r^2 =0.91) between the two datasets is high, particularly considering that Freeborn et al. (2014b) demonstrated a 1σ per-pixel MODIS FRP uncertainty of 27%, based only on variability in the sub-pixel location of the fire itself. Overall, 65% of the per-fire SLSTR-to-MODIS FRP matchups show an FRP difference of less than 50%, and 38% less than 30%, comparable for example to the differences between MODIS FRP retrievals of fires and those made near simultaneously using Meteosat SEVIRI (Roberts et al., 2015).

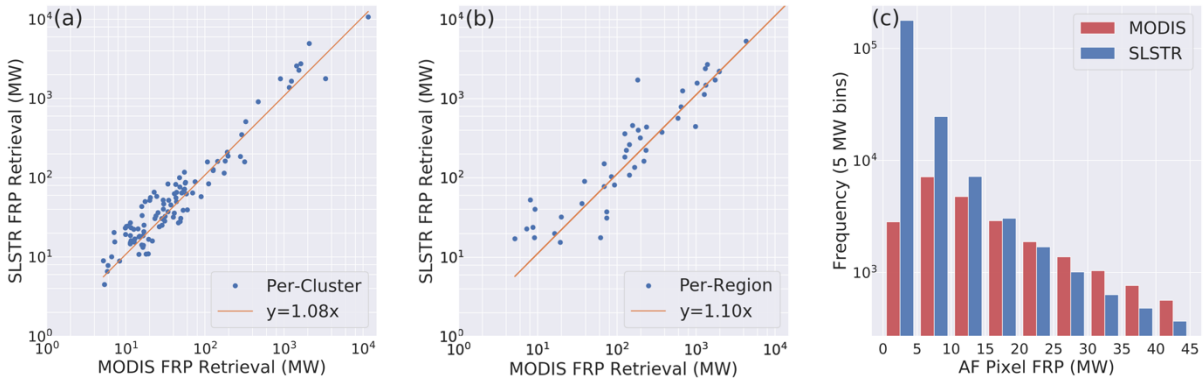

Figure 4. Intercomparison of night-time global FRP records obtained from Sentinel-3 SLSTR and MODIS Terra. (a) per fire cluster comparison and (b) regional comparison, both performed using corresponding SLSTR and MODIS AF products collected within ± 6 minutes of one other and limited to parts of the swath having pixel areas $\leqslant$ 1.7 km^2 – see Section 5.1. (c) FRP frequency distribution, based on all night-time Sentinel-3B and MODIS Terra AF data collected in January 2019 regardless of their imaging time and pixel area – see Section 5.1.

Fig. 4b shows results from the regional FRP intercomparison, based on the total FRP measured within geographical areas imaged by Sentinel-3 SLSTR and by MODIS Terra within

a ±6 minute time of each other (Section 5.1). Each area used for the comparison typically contains multiple fires, in some cases hundreds. As with the per-fire comparison, the Sentinel-3-derived FRP values are typically higher than those of MODIS, again mostly due to the formers ability to detect additional lower FRP pixels. This includes additional AF pixels only detected by SLSTR, as well additional AF pixels detected at the edges of active fire pixel clusters identified by both sensors. For these reasons the slope of the linear best fit to the regional scale data is slightly higher (1.10) than that of the per-fire comparison (1.08) shown in Figure 4a.

Finally, Figure 4c indicates the frequency of night-time AF pixels of different FRPs recorded by Sentinel-3B and by MODIS Terra throughout January 2019, with all SLSTR and MODIS products used regardless of time difference or scan angle. Whilst AF pixels having FRP values between 15 and 25 MW show very similar frequencies, below 15 MW SLSTR detects many more AF pixels than does MODIS. For AF pixels having FRP > 25 MW, which both sensors have no difficulty in detecting, MODIS shows a slightly higher frequency in each FRP class. This is primarily because, more often than not, when MODIS and SLSTR both view the same region at a similar time, MODIS does so with pixels having a larger pixel area (i.e. at the swath edge the MODIS pixel size could be ~10 km^2) which thus can contain "more fire" than can the matching smaller area SLSTR pixels – which may thus be more likely to split the emitted FRP across a number of pixels.

5.4 Exemplar Global Data Record

The complete Sentinel-3B SLSTR night-time AF dataset for January 2019 is mapped at a 1.0° grid cell resolution in Figure 5a (Active Fire Pixel Counts) and 5b (FRP Totals). Shown alongside are data from the same period extracted from the full C6 MODIS Terra 1 km AF

product (MOD14) data record (Figure 5c and 5d), and from the full Suomi NPP VIIRS I-Band 375 m Active Fire product (VNP14IMGTDL) data record (Figure 5e and 5f). As detailed in Section 4.1, these comparison maps include all data from each product for January 2019, regardless of exact night-time overpass time and viewing geometry. Whilst the SLSTR and Terra MODIS data are taken at approximately the same overpass time, those of VIIRS are taken some hours later into the night. Furthermore the data from the single Sentinel-3B satellite used here provide an SLSTR revisit time of approximately two days at the equator, whereas those of VIIRS are daily and those of MODIS Terra are almost daily due to the small orbital gaps in MODIS coverage at the equator (Freeborn et al., 2011; Li et al., 2020).

The maps of Figure 5a and 5c indicate that the SLSTR AF pixel counts for many regions are significantly higher than those from MODIS Terra (see the colour bar scale of Figure 5c), even though the wider MODIS Terra swath provides many more observation opportunities than the does the single Sentinel-3B SLSTR. The spatial patterns of fire appear very similar however, and the grid-cell FRP totals (Figure 5b and 5d) are also similar as a result of the vast majority of additional AF pixels detected by SLSTR having mostly low FRP values (see Section 5.3). Grid cells showing the highest FRP totals result from either large numbers of AF pixels, fires of particularly high FRP, or a combination. Such grid cells include those in and around the Central African Republic, where widespread agricultural, savannah and forest fires occur at this time (Freeborn et al., 2014a), parts of southeast Asia hosting a mixture of agricultural burning and forest clearance (Gaveau et al., 2013), and Australia where large and intense bush fires are relatively frequent at this time of year (Williams et al., 2008). Figure 5e and 5f show respectively the AF counts and FRP totals mapped from VIIRS (VNP14IMGTDL). Due to frequent saturation of the VIIRS 375 m I-Band (I4) MIR channel at

pixels containing active fires, FRP retrievals with VIIRS are made using radiances from the spatially matched, lower-gain and larger area 750 m M-Band (M12) data (Zhang et al., 2017; Schroeder et al., 2018). In terms of AF pixel counts, VIIRS shows again a very similar spatial pattern as depicted by Sentinel-3B SLSTR and by MODIS Terra, though with typically far higher numbers of AF pixels being detected - especially in North America and China. Globally whilst Sentinel-3B SLSTR detects 208,284 night-time AF pixels in total in January 2019, MODIS Terra detects 27,404 and VIIRS 487,884 respectively. If we added the AF detections that would have been made by Sentinel-3A (whose orbit is 140° out of phase from that of Sentinel-3B), this would be expected to approximately double the number of SLSTR active fire pixel counts obtained over the period.

There are competing reasons why the AF pixel counts from VIIRS are very different from those of SLSTR and MODIS Terra. The far smaller pixel area of the VIIRS I-Band means that active fires with a lower FRP than those identifiable with SLSTR and MODIS can be discriminated by VIIRS, and also that larger active fires will be split into a greater number of (smaller) AF pixels for VIIRS than for SLSTR or MODIS (see Zhang et al., 2017). However, Suomi NPP crosses areas at night typically at times closer to the minimum of the fire diurnal cycle than does Sentinel-3 and Terra (Giglio et al., 2007), and there are issues of overcounting of the I-Band AF pixel counts with VIIRS in some areas due to high AF detection false alarm rates, most notably in China (Schroeder et al., 2014; Zhang et al., 2017). Like the AF pixel count, the FRP totals from VIIRS are much higher than those of SLSTR due to its higher spatial resolution. Globally whilst Sentinel-3B SLSTR detects a total FRP of 1,335,436 MW throughout January 2019, MODIS detects 931,032 MW and VIIRS

4,049,032 MW respectively. Again, including Sentinel-3A data would be expected to approximately double the total FRP recorded by the SLSTR dataset.

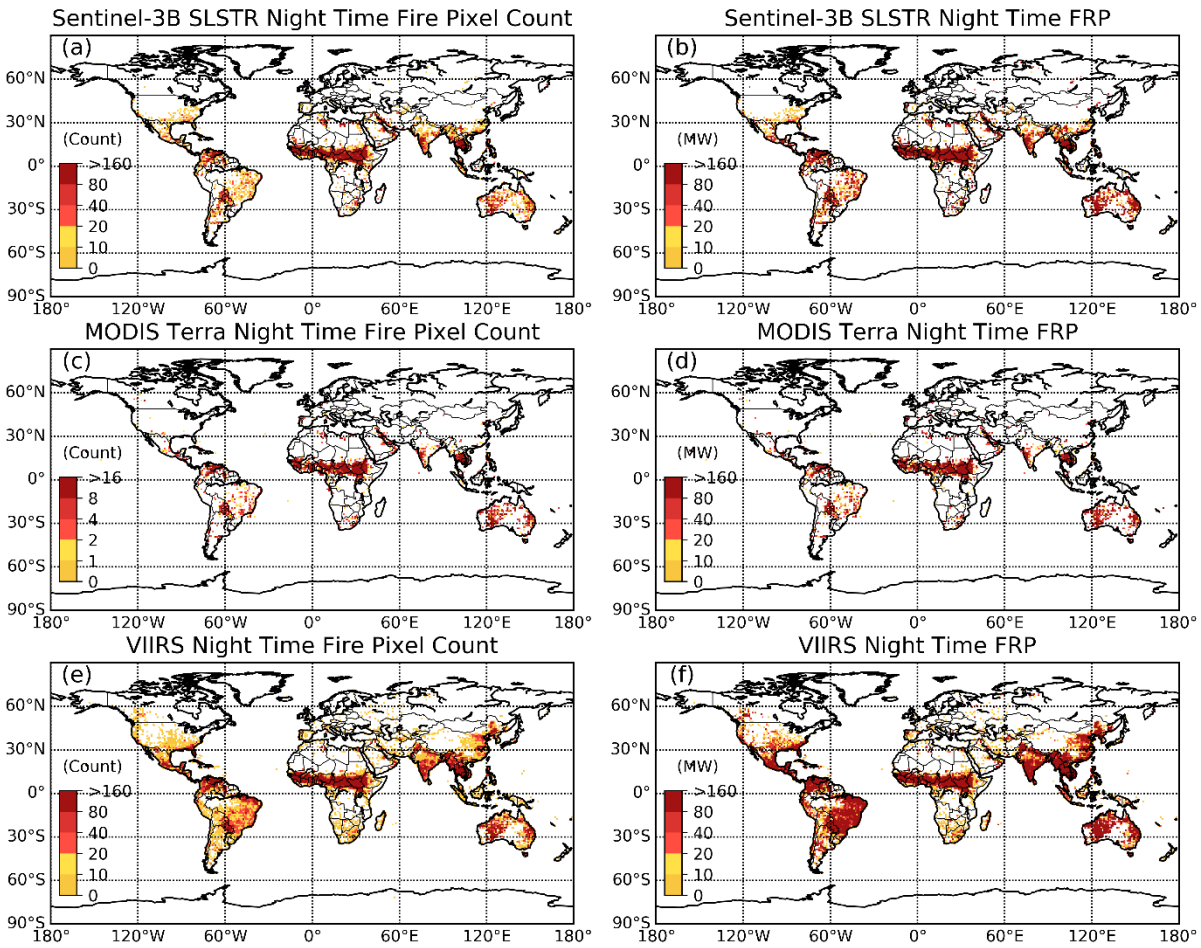

Figure 5. Total active fire pixel count and total FRP of actively burning fires detected within 1° grid cells using Sentinel-3B SLSTR, MODIS Terra and Suomi NPP VIIRS data of January 2019. (a) SLSTR AF pixel count; (b) SLSTR total FRP; (c) MODIS Terra AF pixel count; (b) MODIS Terra total FRP; (e) VIIRS 375 m AF pixel count; (f) VIIRS total FRP. Note different colour bar scale for (c), and that whilst VIIRS provides observations each night, MODIS provides a slightly lower imaging frequency and Sentinel-3B around half this. These descriptions apply to equatorial regions and the imaging frequency for all sensors will increase at higher latitudes.

518 Some areas of clear difference do exist between the SLSTR- and MODIS-derived FRP records
519 shown in Figure 5, even though these two datasets are based on observations made at very
520 similar times of the night. For example, in south-eastern regions of the USA and China, in
521 Spain and central Australia. Whilst Figure 5 uses all night-time Sentinel-3B SLSTR and MODIS
522 Terra data regardless of scan angle or differences in their exact imaging times, in some
523 regions the sensors image at almost the same time and in this case the causes of the
524 differences can be further examined in the absence of significantly changed fire activity
525 between the two views. Figure 6 shows one such example, from south-eastern USA, where
526 Figure 5a and 5c indicate that SLSTR identifies many AF pixels which remain undetected by
527 MODIS Terra. These fires were identified using SLSTR data collected relatively close to the
528 swath centre (Figure 6b; S7 pixel area $\leqslant$ 1.3 km^2), whilst MODIS mostly imaged the area
529 (Figure 6a) at scan angles in excess of 40° (Figure 6c; pixel area > 2.6 km^2). This difference
530 means that the MODIS view had a far higher minimum FRP detection limit than the SLSTR
531 view, explaining the difference seen in this region in Figure 5. Figure 6d confirms that
532 signatures from the AF pixels detected by SLSTR also show up in the instruments 2.2 µm
533 shortwave infrared channel (S6), meaning they are very unlikely to be false alarms as night-
534 time signals in this channel are only found over high temperature targets (Fisher and
535 Wooster, 2019).

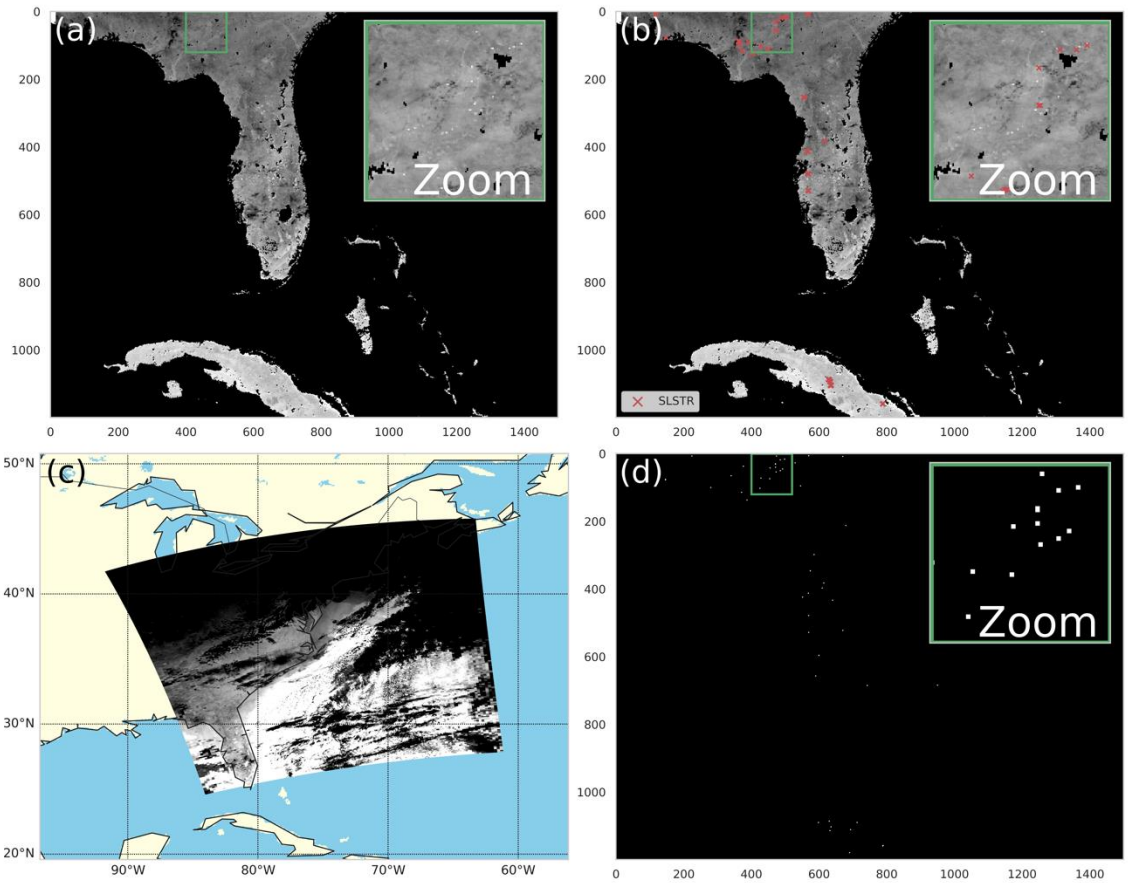

536

537 **Figure 6.** Detail of fires burning at night in southeast USA and Cuba on 9th January 2019,
538 which in Figure 5 appears to have been well detected by Sentinel-3B SLSTR but far less so by
539 MODIS Terra. The SLSTR and MODIS data happen to be collected almost simultaneously (
540 03:11 and 03:05 UTC respectively), meaning that the differences seen in Figure 5 are not
541 likely due to variations in actual fire activity on the ground, but rather appear due to MODIS
542 imaging the area with significantly larger pixels than SLSTR. (a) SLSTR MIR-LWIR (S7 – S8) BT
543 difference image (Kelvin), where pixels containing actively burning fires typically have higher
544 (brighter) values. Most of the fires lie relatively close to the SLSTR swath centre; (b) same as
545 (a) but with SLSTR AF pixel detections superimposed as red dots (with a one pixel offset for
546 clarity); (c) MODIS Terra MIR (band 21) – LWIR (band 31) BT difference (K) image of a similar
547 area as (a), showing that the active fire regions in (a) appear to be imaged close to the MODIS

548 swath edge; (d) SLSTR SWIR (S6 channel) spectral radiance image of the same region. At night
549 SWIR signals over the ambient background are close to zero, and pixels showing a signal of
550 0.15 $W \cdot m^{-2} \cdot sr^{-1} \cdot \mu m^{-1}$ or higher are very likely to contain actively burning fires or other high
551 temperature sources such as gas flares. Their presence therefore acts as confirmation that
552 the AF detections made here are due to real high temperature events and not false alarms.

553 Figure 7 shows the time series of regional AF pixel count and total FRP derived by SLSTR and
554 MODIS throughout January 2019 for four fire affected $5^o \times 5^o$ areas over South American,
555 Africa and Asia. Again, as described in Section 5.1 all night-time data are used regardless of
556 exact observation time or scan angle. The location of each of the four regions is marked in
557 yellow in Figure A1 (Appendix A), and for each the temporal patterns seen in the SLSTR- and
558 MODIS-derived AF datasets are very similar, but SLSTR typically detects many more times
559 the number of active fires than does MODIS, agreeing with the findings of Section 5.3 and
560 5.4. However, since these additional AF pixel detections are mostly associated with low FRP
561 values, being located either in smaller AF clusters or at the edges of larger fire cluster, the
562 total FRP assessed by SLSTR is far more similar to that provided by MODIS than are the
563 numbers of AF detections.

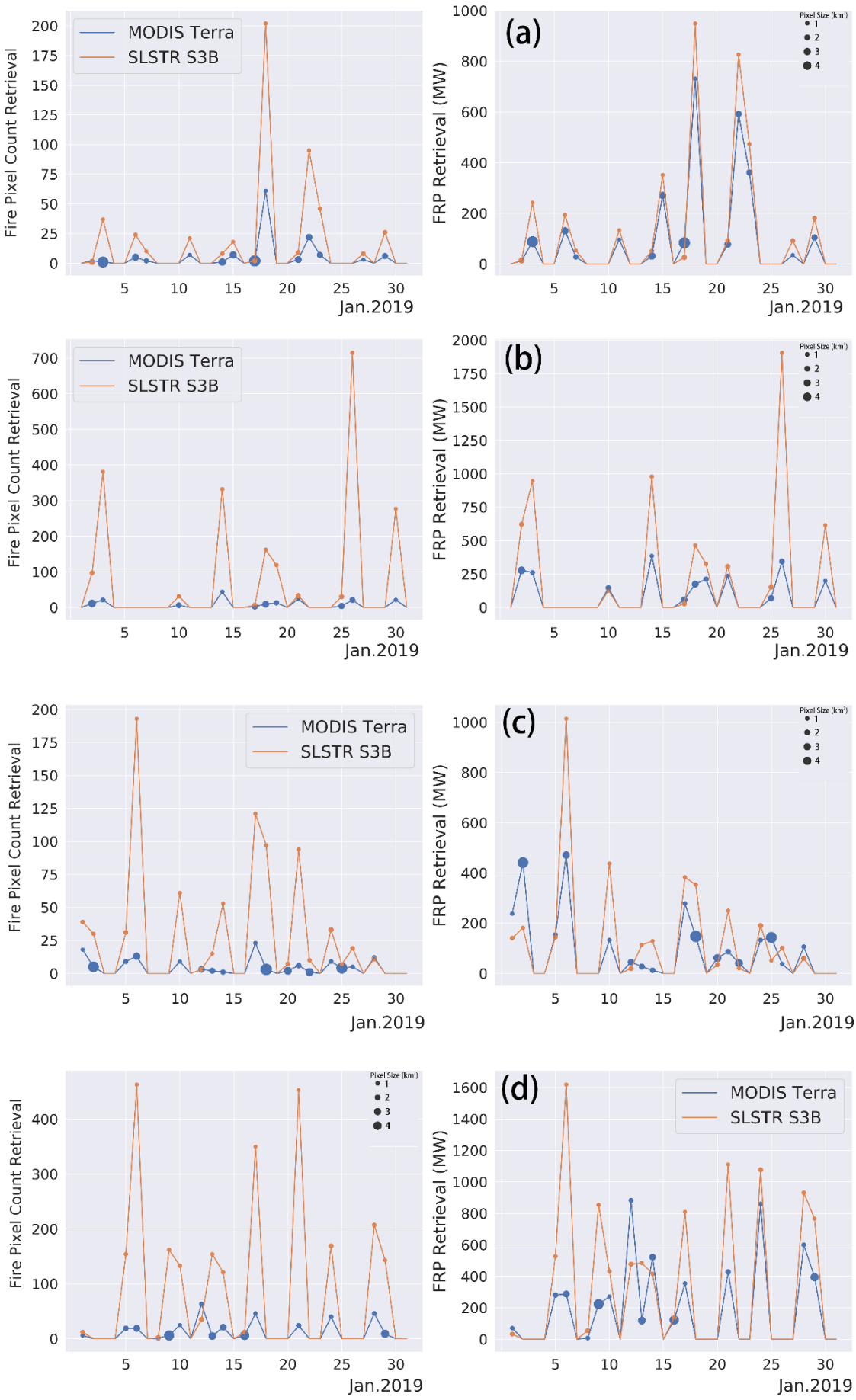
(a)
(b)
(c)
(d)
MODIS Terra
SLSTR S3B
Fire Pixel Count Retrieval
FRP Retrieval (MW)
Jan.2019
Pixel Size (km²)
1
2
3
4

Figure 7. Time Series of total regional AF pixel count (left) and total FRP (right) measured in four different $5^o \times 5^o$ grid cells located in different geographical regions (see Figure A1 of Appendix A for exact location). Data come from Sentinel-3B SLSTR and MODIS Terra in January 2019. Those days having no Sentinel-3B or MODIS Terra observations are reported as zeros, and the size of the dots represents the mean pixel area (F1 for SLSTR; Band 21 for MODIS) of the sensor over the region being targeted. MODIS commonly has a pixel area double that of SLSTR. Across all four regions, SLSTR typically detects on average around 5 × the number of AF fires and 1.5 × of the FRP as does MODIS. The location of each region is marked in Figure A1 of APPENDIX A.

6. Summary and Conclusion

The Sea and Land Surface Temperature Radiometer (SLSTR) is collecting Earth observations from two concurrently operating low-Earth orbiting satellites, Sentinel-3A and -3B. The two SLSTR's provide observations across the VIS-to-LWIR spectral range at an equatorial nadir local solar time of ~10:00 am and ~10:00 pm which can be used for active fire detection and FRP retrieval. These data are expected to continue the AF data record made over the past ~ 20 years from MODIS Terra at similar local overpass time. SLSTR possesses specially designed 'fire' [F] channels in the MIR and LWIR, enabling global characterisation of landscape fire FRP over even strongly burning fires without detector saturation. The pre-launch SLSTR active fire (AF) detection and FRP retrieval algorithm of Wooster et al. (2012) has been significantly updated now that real SLSTR data are available, with an AF pixel clustering approach being the most significant addition. We have assessed the performance of the updated algorithm using some Sentinel-3A scenes as well as global Sentinel-3B data from January 2019, and have compared these to the 1 km active fire data products available

588 from MODIS Terra and from VIIRS 375 m I-Band. We have focused on night-time data only,
589 since certain of the SLSTR detector characteristics means that daytime AF detection and FRP
590 retrieval will require further algorithm adjustments. Note that fire activity typically shows a
591 strong diurnal cycle, and with a minima at night in term of both active fire count (Giglio et
592 al., 2007) and FRP (Roberts et al., 2009). So, even though the diurnal fire cycle minima
593 typically occur some hours after the local Sentinel-3 overpass time, it remains the case that
594 the night-time AF fire counts and FRP totals provided by SLSTR at night are likely to be a
595 small proportion of those that would be measured by day. A daytime version of the
596 Sentinel-3 AF product is expected to be released in 2021.

597 Our results show that near simultaneous views of the same fire made by SLSTR and by
598 MODIS provide very similar FRP retrievals, though overall SLSTR provides slightly higher
599 values (~ 8%; based on a least squares linear best-fit to multiple per-fire comparison data)
600 due to its ability to identify lower FRP pixels burning at the edges of AF pixel clusters. At the
601 regional scale, SLSTR provides a further increase on MODIS' FRP values (to ~ 10%) due to the
602 same effect plus that of additionally detected low FRP active fire pixels that remain
603 unidentified by MODIS. Overall in our matchup dataset, SLSTR detects 90% of the MODIS-
604 detected AF pixels, plus a further 44% where MODIS provides no AF detection at all. The
605 vast majority of these additional AF pixels have FRP < 5 MW, indicating the somewhat lower
606 minimum FRP detection limit of the SLSTR AF product than the MODIS AF product. Analysis
607 of global night-time Sentinel-3B SLSTR and MODIS AF fire data for January 2019 shows that
608 the former detects around 7× more AF pixels than does MODIS, though their FRP totals
609 calculated at 1° grid cell resolution are rather similar since the additional SLSTR-detected AF
610 pixels each generally have a low FRP.

With the orbit of MODIS Terra to be lowered in the coming years and the spacecraft and instrument being well beyond its design life, Sentinel-3 is expected to become the primary provider of mid-morning and early night-time global AF data, with near-real time production occurring within 3 hrs of data capture. The results shown herein demonstrate the capabilities of the SLSTR night-time AF detection and FRP retrieval capability, with the near real-time (NRT) product produced within 3 hrs of data collection and available through fast-delivery routes (https://www.eumetsat.int/website/home/Satellites/CurrentSatellites/Sentinel3/AtmosphericComposition/index.html). The non time critical (NTC) data products will be available for example through the Sentinel-3 Data Hub (https://scihub.copernicus.eu/s3) which we expect to start delivering data operationally to users in the second half of 2020. The full daytime version of the product will follow in 2021.

Reference

Andreae, M. O. (1991). Biomass burning: Its history, use and distribution, and its impact on envi- ronmental quality in global climate. In J. Levine (Ed.), Global biomass burning: Atmosphere, climatic, and biospheric implications, pp. 3–21. Cambridge, MA: MIT Press.

Andela, N., Kaiser, J.W., Van der Werf, G.R., & Wooster, M.J. (2015). New fire diurnal cycle characterizations to improve fire radiative energy assessments made from MODIS observations. *Atmospheric Chemistry and Physics*, 15, 8831-8846

Andela, N., Morton, D. C., Giglio, L., Chen, Y., Van Der Werf, G. R., Kasibhatla, P. S., Defries, R. S., Collatz, G. J., Hantson, S., Kloster, S., Bachelet, D., Forrest, M., Lasslop, G., Li, F.,

632 Mangeon, S., Melton, J. R., Yue, C., and Randerson, J. T. (2017). A human-driven decline in
633 global burned area, *Science*, 356, 1356–1362

634 Arino, O. and Rosaz, J.M. (1999). 1997 and 1998 world ATSR fire atlas using ERS-2 ATSR-2 data.
635 In *Proc. Joint Fire Sci.* Conf (pp. 177-182). Boise, ID.

636 Bowman, D.M.J.S., Balch, J.K., Artaxo, P., Bond, W.J., Carlson, J.M., Cochrane, M.A., D'Antonio,
637 C.M., DeFries, R.S., Doyle, J.C., Harrison, S.P., Johnston, F.H., Keeley, J.E., Krawchuk, M.A.,
638 Kull, C.A., Marston, J.B., Moritz, M.A., Prentice, I.C., Roos, C.I., Scott, A.C., Swetnam, T.W.,
639 Van der Werf, G.R., & Pyne, S.J. (2009). Fire in the Earth System. *Science*, 324, 481-484

640 Coppo, P., Ricciarelli, B., Brandani, F., Delderfield, J., Ferlet, M., Mutlow, C., et al. (2010).
641 SLSTR: A high accuracy dual scan temperature radiometer for sea and land surface
642 monitoring from space. *Journal of Modern Optics*, 57(18), 1815–1830 October 2010

643 Coppo, Peter, Dave Smith, and Jens Nieke (2015). Sea and Land Surface Temperature
644 Radiometer on Sentinel-3. in *Optical Payloads for Space Missions* (2015), Shen-En Qian (ed),
645 pp. 701-714.

646 Delderfield, J., Llewellyn-Jones, D.T., Bernard, R., De Javel, Y., Williamson, E.J., Mason, I., Pick,
647 D.R. and Barton, I.J. (1986). The along track scanning radiometer (ATSR) for ERS1.
648 In *Instrumentation for Optical Remote Sensing from Space* (International Society for Optics
649 and Photonics)., 589, 114-120.

650 Dillencourt M. B., Samet H., Tamminen M. (1992). A general approach to connected-
651 component labeling for arbitrary image representations. *Journal of the ACM*. 39 (2): 253

652 Freeborn, P.H., Wooster, M.J. and Roberts, G. (2011), Addressing the spatiotemporal sampling design
653 of MODIS to provide estimates of the fire radiative energy emitted from Africa. *Remote Sensing of*
654 *Environment*, *115*, 475-489.

655 Freeborn, P.H., Wooster, M.J., Hao, W.M., Ryan, C.A., Nordgren, B.L., Baker, S.P. and Ichoku, C., 2008.
656 Relationships between energy release, fuel mass loss, and trace gas and aerosol emissions during
657 laboratory biomass fires. Journal of Geophysical Research: Atmospheres, 113(D1).

658 Freeborn, P.H., Wooster, M.J., Roberts, G., & Xu, W.D. (2014a). Evaluating the SEVIRI Fire Thermal
659 Anomaly Detection Algorithm across the Central African Republic Using the MODIS Active Fire
660 Product. *Remote Sensing, 6*, 1890-1917

661 Freeborn, P.H., Wooster, M.J., Roy, D.P. and Cochrane, M.A. (2014b). Quantification of MODIS fire
662 radiative power (FRP) measurement uncertainty for use in satellite-based active fire characterization
663 and biomass burning estimation. *Geophysical Research Letters*, *41*, 1988-1994.

664 Giglio, L. (2007). Characterization of the tropical diurnal fire cycle using VIRS and MODIS observations.
665 *Remote Sensing of Environment, 108*, 407-421

666 Giglio L., Descloitres J., Justice C.O., Kaufman Y.J (2003). An Enhanced Contextual Fire Detection
667 Algorithm for MODI. *Remote Sensing of Environment*, *87*, 273-282,

668 Giglio, L., Schroeder, W., & Justice, C.O. (2016). The collection 6 MODIS active fire detection algorithm
669 and fire products. *Remote Sensing of Environment, 178*, 31-41

670 Giglio, L., Kendall, J.D. and Justice, C.O. (1999). Evaluation of global fire detection algorithms using
671 simulated AVHRR infrared data. *International Journal of Remote Sensing*, 20(10), pp.1947-1985.

672 Ichoku, C., & Ellison, L. (2014). Global top-down smoke-aerosol emissions estimation using satellite fire
673 radiative power measurements. *Atmospheric Chemistry and Physics, 14*, 6643-6667

674 Johnston, F., Hanigan, I., Henderson, S., Morgan, G., & Bowman, D. (2011). Extreme air pollution events
675 from bushfires and dust storms and their association with mortality in Sydney, Australia 1994–2007.
676 *Environmental Research, 111*, 811-816

677 Justice, C. O., Kendall, J. D., Dowty, P. R., and Scholes, R. J. (1996), Satellite remote sensing of fires
678 during the SAFARI campaign using NOAA Advanced Very High Resolution Radiometer data, *J.*
679 *Geophys. Res*., 101(D19), 23851– 23863, doi:10.1029/95JD00623.

680 Kaiser, J.W., Heil, A., Andreae, M.O., Benedetti, A., Chubarova, N., Jones, L., Morcrette, J.J., Razinger,
681 M., Schultz, M.G., Suttie, M., & van der Werf, G.R. (2012). Biomass burning emissions estimated with
682 a global fire assimilation system based on observed fire radiative power. *Biogeosciences, 9*, 527-554

683 Kaufman, Y.J., Justice, C.O., Flynn, L.P., Kendall, J.D., Prins, E.M., Giglio, L., Ward, D.E., Menzel, W.P.
684 and Setzer, A.W. (1998) Potential global fire monitoring from EOS-MODIS. *Journal of Geophysical*
685 *Research: Atmospheres*. 103(D24). 32215-32238.

686 Llewellyn-Jones, D., Edwards, M. C., Mutlow, C. T., Birks, A. R., Barton, I. J., & Tait, H. (2001). AATSR —
687 Global-change and surface-temperature measurements from Envisat. *ESA Bulletin*, 105,11–21 (ISSN
688 0376-4265)

689 Li, F., Zhang, X. and Kondragunta, S. (2020). Biomass Burning in Africa: An Investigation of Fire Radiative
690 Power Missed by MODIS Using the 375 m VIIRS Active Fire Product. *Remote Sensing*, 12, 1561.

691 Mota, B. and Wooster, M.J, (2018). A new top-down approach for directly estimating biomass burning
692 emissions and fuel consumption rates and totals from geostationary satellite fire radiative power
693 (FRP). *Remote Sensing of Environment*, 206, 45-62.

694 Natarajan, M., Pierce, R.B., Schaack, T.K., Lenzen, A.J., Al-Saadi, J.A., Soja, A.J., Charlock, T.P., Rose, F.G.,
695 Winker, D.M., & Worden, J.R. (2012). Radiative forcing due to enhancements in tropospheric ozone

and carbonaceous aerosols caused by Asian fires during spring 2008. *Journal of Geophysical Research-Atmospheres, 117*

Randerson, J.T.; Chen, Y.; Werf, G.R.; Rogers, B.M.; Morton, D.C. Global burned area and biomass burning emissions from small fires. *J. Geophys. Res. Biogeosci*. 2012, 117.

Reid, J.S., Hyer, E.J., Johnson, R.S., Holben, B.N., Yokelson, R.J., Zhang, J., Campbell, J.R., Christopher, S.A., Di Girolamo, L., Giglio, L., Holz, R.E., Kearney, C., Miettinen, J., Reid, E.A., Turk, F.J., Wang, J., Xian, P., Zhao, G., Balasubramanian, R., Chew, B.N., Janjai, S., Lagrosas, N., Lestari, P., Lin, N.-H., Mahmud, M., Nguyen, A.X., Norris, B., Oanh, N.T.K., Oo, M., Salinas, S.V., Welton, E.J., & Liew, S.C. (2013). Observing and understanding the Southeast Asian aerosol system by remote sensing: An initial review and analysis for the Seven Southeast Asian Studies (7SEAS) program. *Atmospheric Research, 122*, 403-468

Roberts, G.J., & Wooster, M.J. (2008). Fire detection and fire characterization over Africa using Meteosat SEVIRI. *Ieee Transactions on Geoscience and Remote Sensing, 46*, 1200-1218

Roberts, G., Wooster, M. J., & Lagoudakis, E. (2009). Annual and diurnal african biomass burning temporal dynamics. *Biogeosciences*, 6(5), 849-866.

Roberts, G., Wooster, M. J., Xu, W., Freeborn, P. H., Morcrette, J. J., Jones, L, Benedetti A. & Kaiser, J. (2015). LSA SAF Meteosat FRP Products: Part 2--Evaluation and demonstration of use in the Copernicus Atmosphere Monitoring Service (CAMS). *Atmospheric Chemistry & Physics*, 15(22), pp.13241-13267.

Robinson, J.M. (1991) Fire from space: Global fire evaluation using infrared remote sensing. *International Journal of Remote Sensing*, 12(1), pp.3-24.

717 Schroeder, W., Oliva, P., Giglio, L., & Csiszar, I. A. (2014). The New VIIRS 375 m active fire detection
718 data product: Algorithm description and initial assessment. *Remote Sensing of Environment*, 143, 85-
719 96.

720 Schoeder, W. and Giglio. L. (2018) NASA VIIRS Land Science Investigator Processing System (SIPS)
721 Visible Infrared Imaging Radiometer Suite (VIIRS) 375 m & 750 m Active Fire Product User Guide,
722 Available online: https://lpdaac.usgs.gov/documents/427/VNP14_User_Guide_V1.pdf (accessed on
723 4 June 2020).

724 van der Werf, G.R., Randerson, J.T., Collatz, G.J., Giglio, L., Kasibhatla, P.S., Arellano, A.F., Olsen, S.C., &
725 Kasischke, E.S. (2004). Continental-scale partitioning of fire emissions during the 1997 to 2001
726 El Nino/La Nina period. *Science, 303*, 73-76

727 Voulgarakis, A., & Field, R.D. (2015). Fire Influences on Atmospheric Composition, Air Quality and
728 Climate. *Current Pollution Reports, 1*, 70-81

729 Wooster, M.J., Zhukov, B., & Oertel, D. (2003). Fire radiative energy for quantitative study of biomass
730 burning: derivation from the BIRD experimental satellite and comparison to MODIS fire products.
731 *Remote Sensing of Environment, 86*, 83-107

732 Wooster, M. J., Roberts, G., Perry, G. L. W., & Kaufman, Y. J. (2005). Retrieval of biomass combustion
733 rates and totals from fire radiative power observations: FRP derivation and calibration relationships
734 between biomass consumption and fire radiative energy release. Journal of Geophysical Research:
735 Atmospheres, 110(D24).

736 Wooster, M. J., Xu, W., & Nightingale, T. (2012). Sentinel-3 SLSTR active fire detection and FRP product:
737 Pre-launch algorithm development and performance evaluation using MODIS and ASTER datasets.
738 *Remote Sensing of Environment*, 120(0), 236–254.

739 Wooster, M.J., Roberts, G., Freeborn, P.H., Xu, W., Govaerts, Y., Beeby, R., He, J., Lattanzio, A., &
740 Mullen, R. (2015). Meteosat SEVIRI Fire Radiative Power (FRP) products from the Land Surface
741 Analysis Satellite Applications Facility (LSA SAF) – Part 1: Algorithms, product contents and analysis.
742 *Atmos. Chem. Phys. Discuss., 15*, 15831-15907

743 Xu, W., Wooster, M.J., Roberts, G., & Freeborn, P. (2010). New GOES imager algorithms for cloud and
744 active fire detection and fire radiative power assessment across North, South and Central America.
745 *Remote Sensing of Environment, 114*, 1876-1895

746 Xu, W., Wooster, Kaneko T., He J., Zhang T., Fisher D. (2017). Major advances in geostationary fire
747 radiative power (FRP) retrieval over Asia and Australia stemming from use of Himarawi-8 AHI.
748 *Remote Sensing of Environment,* 193, 138-149

749 Wooster, M.J., Roberts, G., Smith, A.M., Johnston, J., Freeborn, P., Amici, S. and Hudak, A.T. (2013).
750 Thermal remote sensing of active vegetation fires and biomass burning events. In *Thermal Infrared*
751 *Remote Sensing* (pp. 347-390). Springer, Dordrecht.

752 Zhukov, B., Lorenz, E., Oertel, D., Wooster, M., & Roberts, G. (2006). Spaceborne detection and
753 characterization of fires during the bi-spectral infrared detection (BIRD) experimental small satellite
754 mission (2001–2004). *Remote sensing of Environment*, 100(1), 29-51.

755 Zhang, T., Wooster, M. J., & Xu, W. (2017). Approaches for synergistically exploiting VIIRS I-and M-Band
756 data in regional active fire detection and FRP assessment: A demonstration with respect to
757 agricultural residue burning in Eastern China. *Remote Sensing of Environment*, 198, 407-424.

758 Zhang, T., Wooster, M., de Jong, M., & Xu, W. (2018). How Well Does the 'Small Fire Boost'
759 Methodology Used within the GFED4. 1s Fire Emissions Database Represent the Timing, Location
760 and Magnitude of Agricultural Burning? *Remote Sensing*, 10(6), 823.

761

APPENDIX A

Subsequent to the availability of real SLSTR data from Sentinel-3A and -3B, key changes to the active fire detection thresholds and to a few of the other details of the pre-launch algorithm of Wooster et al. (2012) were required. These adjustments were made based on detailed examination of eight scenes processed with the night-time AF detection algorithm reported herein and collected by Sentinel-3A over Canada, America, Europe and Africa (Table A1; Fig. A1). These scenes were selected as they have enough fires at night and cover a wide set of fire regimes. Examination of the full January 2019 SLSTR AF dataset shown herein and produced with this algorithm indicated that no further adjustment of the thresholds were required. The final algorithm workflow (Figure A2) is essentially the same as in Wooster et al., (2012) with the major addition of the AF pixel clustering stage, but with details enhanced and optimised as discussed below.

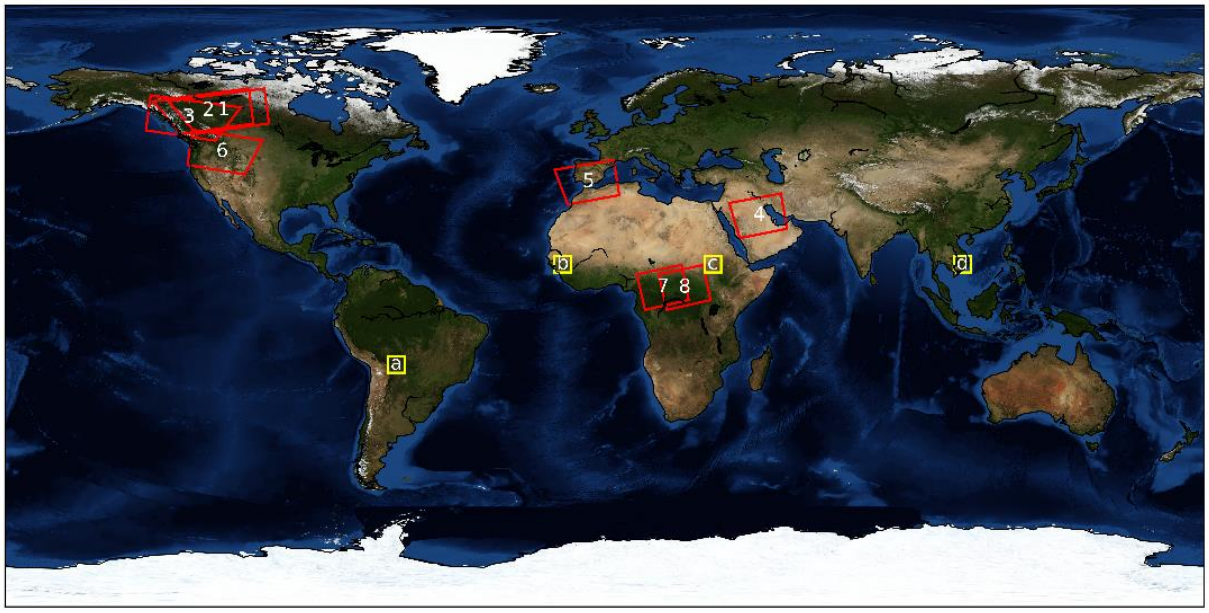

Figure A1. Location of the eight Sentinel-3A SLSTR data granules (red) used to optimize the contextual active fire detection thresholds of the Wooster et al. (2012) algorithm (detailed in Table A1). Also outlined in yellow are the locations of the four 5º × 5º areas used to

generate the SLSTR and MODIS AF and FRP times series data shown in Figure 7 of the main paper

Table A1. Date and location of the eight Sentinel-3A SLSTR data granules used to test and optimize the thresholds of the Wooster et al. (2012) SLSTR AF detection algorithm whose details and performance are enhanced herein. Figure A1 maps the locations of these granules.

Granule No	Day	Time	Mean Latitude (°)	Mean Longitude (°)
1	20160506	045622	58.46	-114.32
2	20160513	051504	58.43	-118.98
3	20160521	185329	56.42	-124.78
4	20160528	184511	27.02	46.43
5	20170618	220243	37.11	-4.75
6	20171118	180025	46.15	-114.73
7	20180103	205352	5.55	17.58
8	20180104	202741	5.54	24.13

The thresholds used in the pre-launch algorithm tests of Wooster et al. (2012) were found to works generally quite well, and relatively few changes were required. Table A2 details the changes made to the algorithm workflow outlined in Figure 5 of Wooster et al. (2012) and an update version of that flowchart is shown as Figure A2.

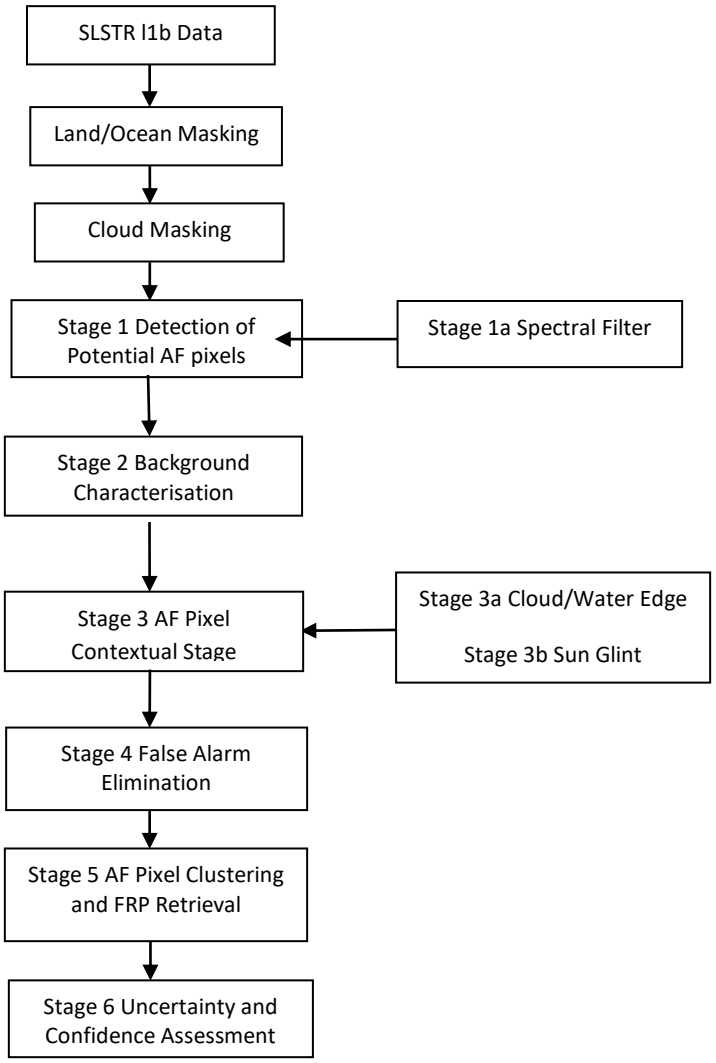

789

790 Figure A2. Structure of the SLSTR nighttime Fire Detection and Characterisation algorithm.
791 Note the algorithm has been updated and enhanced from the pre-launch version presented
792 in Wooster *et al.* (2012), for example introducing the AF pixel clustering approach detailed
793 in the main paper, a cloud/water edge test similar to that in Wooster et al. (2015) to reduce
794 the incidence of false alarms close to water bodies and clouds, and employing a gross cloud
795 mask based on that of Giglio et al. (2003).

After the SLSTR level 1b data are read in, the 'cosmetic fill' pixels (see https://sentinel.esa.int/web/sentinel/technical-guides/sentinel-3-slstr/level-1/cosmetic-fill) are masked out. Test 2c in Wooster et al. (2012) was removed as it sometimes removed true AF pixels yet provided not benefits. A new cloud/water edge test similar to that in Wooster et al. (2015) was introduced to reduce the incidence of false alarms close to water bodies and clouds, and we employed a set of very simple tests from Giglio et al. (2003) (used in the MODIS AF products) to mask out gross cloud cover. Finally, we introduced an atmospheric correction procedure into the FRP retrieval, based on an atmospheric transmittance calculation and the approach used with the Meteosat SEVIRI FRP product (Wooster et al., 2015).

Table A2. Details of the SLSTR nighttime active fire detection and FRP retrieval algorithm described in Wooster et al. (2012) and updated herein, along with changes made compared to the pre-launch algorithm of Wooster et al. (2012). The Algorithm Stage is that illustrated in Figure A2, and test numbers here also refer to those described in Wooster et al. (2012).

Algorithm Stage	Change or Updated Threshold	Detail of Any Changes
Level 1b Data ingestion	Wooster et al. (2012) used only MODIS data.	Algorithm now works with SLSTR Level 1B data, with cosmetic fill pixels removed prior to AF detection.
Cloud Masking	$BT_{S8} < 273K$ BT_{S8} is the pixel brightness temperature (BT) in the S8 channel (Kelvin).	This very basic cloud mask test is applied to remove pixels showing gross cloud contamination. Test based on that from the MODIS fire products described in Giglio et al. (2003).

Spectral Filter Test	$BT_{S7} > \overline{BT}_{S7}^{cf}$ $\Delta BT_{S7-S8} > \Delta\, \overline{BT}_{S7-S8}^{cf}$ BT_{S7} is the BT in the S7 channel; $\overline{BT}_{S7}^{cf}$ is the mean BT in the S7 channel at clear land background pixels; ΔBT_{S7-S8} is the BT difference between S7 and S8; $\Delta\overline{BT}_{S7-S8}^{cf}$ is mean BT difference between S7 and S8 from clear land background pixels.	Test 2c in Wooster et al. (2012) has been removed as we found it prevented some active fires being detected at night.
Background Characterisation	$BT_{S7,\,w} < BT_{S7,\,pf}$ $\Delta BT_{S7\text{-}S8,w} < \Delta BT_{S7\text{-}S8,\,pf}$ $BT_{S7,w} < 310$ k $\Delta BT_{S7\text{-}S8,w} < 20$ K $\theta_g < 2$ ° $BT_{S7,\,w}$ is the BT of the background pixel, $BT_{S7,\,pf}$ is the BT of the potential fire, $\Delta BT_{S7\text{-}S8}$,w is BT difference between S7 and S8 of the background pixel, $\Delta BT_{S7\text{-}S8,pf}$ is BT difference between S7 and S8 of the potential fire pixel, θ_g is sun glint angle.	No Change

Absolute Threshold Test	$BT_{F1} > 326$ K BT_{F1} is the BT from F1 Band.	The detection threshold has increased from 320 K to 326K, as the former resulted in some flase alarms at night (possibly due to occasional instrument issues recording anomalously warm pixels in F1). Test 5b in Wooster et al. (2012) is not applied herein as we concentrated on AF detection with MIR and LWIR bands, not the SWIR bands.
Contextual Test	$\Delta BT_{S7-S8} > \Delta\overline{BT}_{S7-S8} + 3.2 \times \sigma_{\Delta BT_{S7-S8}}$ $\Delta BT_{S7-S8} > \Delta\overline{BT}_{S7-S8} + 5.6$ $BT_{S7} > \overline{BT}_{S7} + 3 \times \sigma_{BT_{S7}}$ ΔBT_{S7-S8} is S7 and S8 BT difference of the potential fire pixel; $\Delta\overline{BT}_{S7-S8}$ is the mean S7 and S8 BT difference of valid background pixels; $\sigma_{\Delta BT_{S7-S8}}$ is the mean absolute deviation of the S7 and S8 BT diffirence from the valid background pixels; $\overline{BT}_{S7}$ is mean S7 BT of the valid background pixels; and $\sigma_{BT_{S7}}$ is the mean absolute deviation of S7 BT of the valid background pixels.	No Change
Cloud/Water Edge Test	If one or more pixels in the 3 × 3 pixel window surrounding the AF pixel are cloud or water, and if the nighttime AF pixel has an S7 BT < 310 K, then the AF pixel is rejected as a Cloud/Water edge false alarm. And $\frac{L_{S7}}{L_{S8}} < 0.05$ and $BT_{S7} < 310$ K L_{S7} and L_{S8} is the radiance from S7 and S8 respectively.	Introduced to minimize false alarms next to cloud and water bodies, in a similar way to that applied in the LSA SAF Meteosat SEVIRI AF product described in Wooster et al. (2015).
Desert Boundary		Removed as unnecessary at night.

Rejection	Not used	
Atmosphere correction of FRP retrieval	$\tau = exp\left(\frac{-\tau}{cos(A+Bq\theta_v+C(q\theta_v)^2)}\right)$ with $q = \pi / 180$. Where Values of A,B,C have been adjusted to fit exactly the variations as a function of satellte view angle (θ_v). τ is the atmosphere transmittance at nadir, which is specificed as a function of total column of water vapour.	Taken from the procedure used to correct the LSA SAF Meteosat SEVIRI AF product for the effects of non-unitary atmospheric transmission, as detailed in Wooster et al. (2015).

811